

## Development of the Normalization Method for the Jagiellonian PET Scanner

A. COUSSAT<sup>a,b,\*</sup>, W. KRZEMIEN<sup>b,c</sup>,  
J. BARAN<sup>a,b</sup> AND S. PARZYCH<sup>a,b</sup>  
FOR THE J-PET COLLABORATION

<sup>a</sup>*Faculty of Physics, Astronomy and Applied Computer Science,  
Jagiellonian University, 30-348 Kraków, Poland,*

<sup>b</sup>*Centre for Theranostics, Jagiellonian University, 31-501 Kraków, Poland,*

<sup>c</sup>*High Energy Physics Division, National Centre for Nuclear Research,  
Otwock, Swierk, PL 05-400, Poland*

Doi: [10.12693/APhysPolA.142.414](https://doi.org/10.12693/APhysPolA.142.414)

\*e-mail: [aurelien.coussat@uj.edu.pl](mailto:aurelien.coussat@uj.edu.pl)

This work aims at applying the theory of the component-based normalization to the Jagiellonian PET scanner, currently under development at the Jagiellonian University. In any positron emission tomography acquisition, efficiency along a line-of-response can vary due to several physical and geometrical effects, leading to severe artifacts in the reconstructed image. To mitigate these effects, a normalization coefficient is applied to each line-of-response, defined as the product of several components. The specificity of the Jagiellonian PET scanner geometry is taken into account. The results obtained from the GATE simulations are compared with the preliminary results obtained from the experimental data.

topics: positron emission tomography (PET), Jagiellonian PET, normalization

### 1. Introduction

The Jagiellonian PET (J-PET) scanner is a high-acceptance multi-purpose positron emission tomography (PET) detector optimized for the detection of photons from positron–electron annihilation, currently under development at the Jagiellonian University [1–4]. The current prototype named the Modular J-PET [5] is composed of 24 individual modules arranged cylindrically. Each module is composed of 13 plastic scintillator strips with a size of  $24 \times 6 \times 500 \text{ mm}^3$ . Scintillators are read out on both sides by a matrix of silicon photomultipliers [1].

Several effects impact the efficiency of the detector strips, such as geometric effects or variations in detector intrinsic efficiencies. To counterbalance the non-uniformity in efficiency, normalization factors can be incorporated into the image reconstruction procedure. This contribution is the first step towards the proper normalization of the Modular J-PET scanner. Section 2 describes the normalization factors and how they are computed, Sect. 3 shows preliminary results, and Sect. 4 concludes briefly.

### 2. Materials and methods

#### 2.1. Normalization coefficients

Proper determination of the normalization coefficient for a given line of response (LOR) permits to compensate for the detector efficiency variation and geometrical effects not included in the projection model. Lack of those corrections leads to artifacts generation and degradation of the final image quality [6]. The so-called component-based normalization method [7] relies on the factorization of the normalization coefficients into sub-components that can be estimated separately, and on using the fan-sum strategy to lower the variance of the estimations. This work adapts the definitions of Pépin et al. [8].

Unlike conventional PET scanners, whose detectors are divided into several crystals, the J-PET scintillator strips are continuous in the axial direction. Nevertheless, we define  $M$  virtual bins in the axial direction. We also denote as  $L$  the number of strips (312 in the case of the Modular J-PET scanner). LOR that joins portion  $u$  of strip  $i$  with portion  $v$  of strip  $j$  is denoted “LOR  $uivj$ ”. These definitions are illustrated in Fig. 1.

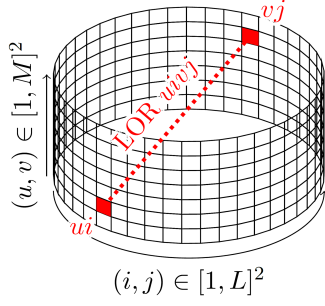


Fig. 1. LOR definition.

The normalization coefficient for a given LOR is given by the product of several normalization factors. Each of these factors accounts for a different effect. The normalization coefficient for LOR  $uivj$  is given as [8]

$$\eta_{uivj} = b_u^{\text{ax}} b_v^{\text{ax}} g_{uv}^{\text{ax}} g_{ij}^{\text{tr}} f_{ij}^{\text{tr}} \epsilon_{ui} \epsilon_{vj}, \quad (1)$$

where  $b^{\text{ax}}$  represents the axial block profile factors,  $g^{\text{ax}}$  represents the axial geometric factors,  $g^{\text{tr}}$  is the transverse geometric factors,  $f^{\text{tr}}$  is the transverse interference function, and  $\epsilon$  represents the intrinsic detector efficiencies. Note that the transverse interference functions are designed to compensate for the non-uniformity of the detection efficiency with respect to the crystal location in the detector block, and they can be ignored in the context of the J-PET scanner due to the design of its detectors.

Axial block profile factors, axial geometric factors, and intrinsic detector efficiencies are computed from the acquisition of a uniform cylindrical source centered on the scanner axis. We denote  $t_{uivj}^{\text{cyl}}$  — the number of true coincidences measured along LOR  $uivj$  during the acquisition. The transverse geometric factors are computed from the acquisition of a uniform annular source, and we denote as  $t_{uivj}^{\text{ann}}$ , the number of true coincidences measured along LOR  $uivj$  during the acquisition. “True coincidences” refer here to coincidences that have not undergone any scattering (in the phantom or in the detector) and that are not accidental.

The axial block profile factors  $b^{\text{ax}}$  normalize the true coincidences along the axial planes, that is, the planes comprising LOR, whose detectors are located at the same axial position ( $u = v$ ). They are defined as

$$b_u^{\text{ax}} = \sqrt{\frac{\frac{1}{M} \sum_{v=1}^M \sum_{i=1}^L \sum_{j=1}^L t_{uivj}^{\text{cyl}}}{\sum_{i=1}^L \sum_{j=1}^L t_{uiuj}^{\text{cyl}}}}. \quad (2)$$

Axial geometric factors account for efficiency variations caused by the detector geometry in the axial direction. They are defined between the two axial positions  $u$  and  $v$  as

$$g_{uv}^{\text{ax}} = \frac{\frac{1}{M^2} \sum_{u'=1}^M \sum_{v'=1}^M b_{u'}^{\text{ax}} b_{v'}^{\text{ax}} \sum_{i=1}^L \sum_{j=1}^L t_{u'iv'j}^{\text{cyl}} \cos(\theta)}{b_u^{\text{ax}} b_v^{\text{ax}} \sum_{i=1}^L \sum_{j=1}^L t_{uivj}^{\text{cyl}} \cos(\theta)}, \quad (3)$$

where  $\theta$  is the angle between LOR and the transverse plane.

Transverse geometric factors also account for the efficiency variations caused by the detector geometry, but this time along the transverse planes. They are defined for the radial distance  $r \in [1; K]$ , where  $K$  is the number of radial bins, as

$$g_r^{\text{tr}} = \frac{\frac{1}{K} \sum_{r'=1}^K \sum_{u=1}^M \sum_{v=1}^M \sum_{i=1}^L \sum_{j=1}^L c_{uivj}^{\text{cyl}}}{\sum_{u=1}^M \sum_{v=1}^M \sum_{i=1}^L \sum_{j=1}^L c_{uivj}^{\text{cyl}}}, \quad (4)$$

where  $x_r(i, j)$  represents the radial distance for the LOR joining strips  $i$  and  $j$ , and where  $c_{uivj}^{\text{ann}}$  represents the number of coincidence for LOR  $uivj$  with the correction given by

$$c_{uivj}^{\text{ann}} = a_{uivj} b_u^{\text{ax}} b_v^{\text{ax}} g_{uv}^{\text{ax}} \epsilon_{ui} \epsilon_{vj} t_{uivj}^{\text{ann}}. \quad (5)$$

Here,  $a_{uivj}$  corresponds to the inverse of the analytical projection of the source.

The intrinsic detector efficiency  $\epsilon_{ui}$  represents the ability of the strip portion located at the ring  $u$  and the strip  $i$  to convert gamma photons into light. This parameter is computed using the fan-sum algorithm as

$$\epsilon_{ui} = \frac{\frac{1}{L} \sum_{i'=1}^L \sum_{v=1}^M \sum_{j=1}^L t_{ui'vj}^{\text{cyl}}}{\sum_{v=1}^M \sum_{j=1}^L t_{uivj}^{\text{cyl}}}. \quad (6)$$

## 2.2. Data acquisition

In order to compute the normalization factors, an acquisition of the Siemens CS-27 cylindrical phantom was performed. The cylinder was 50 cm long, had a radius of 10 cm, and had a capacity of 8407 mL. The cylinder was filled with gallium-68 having an activity of 88.43 MBq and placed at the center of the Modular J-PET. The setup is shown in Fig. 2a. Note that we did not performed any coincidence filtering in this case. At this stage of development, we consider the effect of scattered and accidental coincidences as negligible, and we leave their filtering for future works.

Two simulations of both the cylindrical and the annular phantom were also performed using the GEANT4 Application for Tomographic Emission (GATE) [9]. The cylindrical setup simulates a 1800 s acquisition of the cylinder described above, with an activity of 100 MBq, placed at the center of the detector. The cylindrical simulation setup is illustrated in Fig. 2b. Annular simulation was performed using a moving ring source. The ring source was 1 cm thick and 2.5 mm<sup>3</sup> long with an activity of 10 MBq. A number of 200 positions have been axially simulated, each simulating 100 s of acquisition,

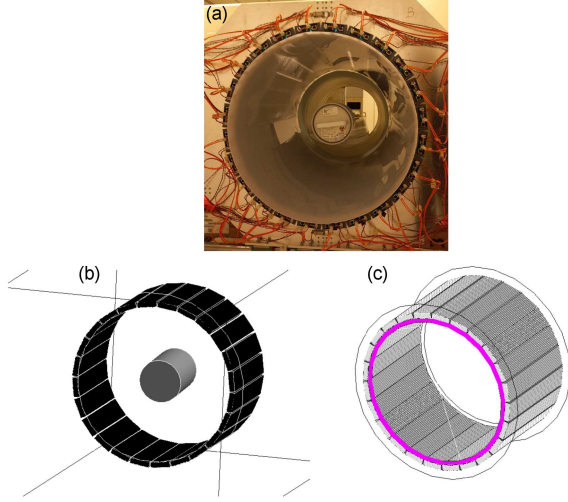


Fig. 2. Data acquisition setups. (a) Data acquisition from a cylindrical phantom. (b) Monte Carlo simulation of a uniform cylindrical phantom. (c) Monte Carlo simulation of a uniform annular phantom (in pink, not to scale).

resulting in a total time of 20000 s. The annular simulation setup is illustrated in Fig. 2c. In both simulations, the scattered and accidental coincidences were completely filtered out based on recorded hit data, resulting in  $5.08 \times 10^7$  true coincidences (out of  $8.77 \times 10^7$  coincidences, 57.90%) for the cylindrical phantom, and  $8.96 \times 10^7$  true coincidences (out of  $1.20 \times 10^8$  coincidences, 74.91%) for the annular phantom.

Values used for the various parameters described in Sect. 2.1 are the following:  $M = 25$ ,  $L = 312$ ,  $K = 25$ .

### 3. Preliminary results

Figure 3 shows the axial geometric factors  $b^{\text{ax}}$ . Lower values near the axial center of the scanner denote higher detection efficiency. The results from Monte Carlo data (Fig. 3a) display stronger fluctuations than those from the real data (Fig. 3b) probably due to lower statistics of the Monte Carlo sample. On the other hand, the factors obtained with the real data are asymmetric — we suppose that this is due to the cylinder being slightly tilted by about  $3^\circ$  during the acquisition. Further investigations are required to conclude this observation.

Figure 4 shows the axial geometric factors  $g^{\text{ax}}$ . As expected from the definition of the axial geometric factors (see (3)), the factors are constant along the diagonal, i.e., where  $u = v$ . At the edges where the ring difference is large, the efficiency is lower due to the decreased probability of LORS, hence the higher values of the axial geometric factors. Note the difference in color scale between Fig. 4a and Fig. 4b — we suggest that these are due to the LOR obliqueness and the coincidence filtering strategy

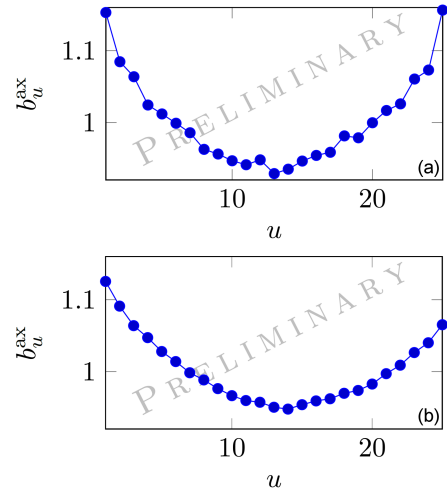


Fig. 3. Axial block profile factors ( $b^{\text{ax}}$ ). The lines between data points illustrate the trend but do not refer to data interpolation. (a) Computed from Monte Carlo data. (b) Computed from cylinder acquisition.

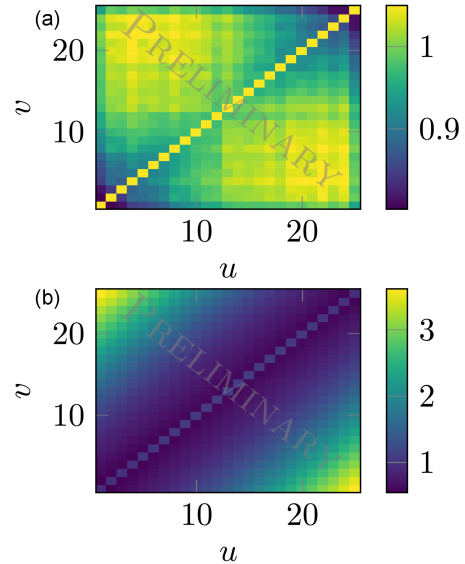


Fig. 4. Axial geometric factors ( $g^{\text{ax}}$ ). (a) Computed from Monte Carlo data. (b) Computed from cylinder acquisition.

applied by the J-PET scanner with respect to the ring difference. However, further investigations are needed to validate our hypothesis.

Figure 5 shows the intrinsic detector efficiencies  $\epsilon$ . In Fig. 5a, since we considered a GATE simulation with perfect detectors and uniform efficiencies, the factors are uniform and the small variations that appear are entirely due to statistical noise. On the other hand, Fig. 5b highlights which areas of the detectors have a lower efficiency. Figure 5c averages on a strip-basis the values presented in Fig. 5b, which makes the anomalies clearly appear.

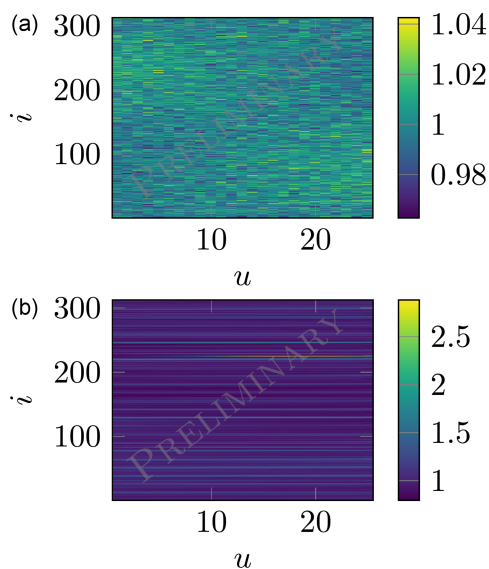


Fig. 5. Intrinsic detector efficiencies ( $\epsilon$ ). (a) Computed from Monte Carlo data. (b) Computed from cylinder acquisition. (c) Average value of  $\epsilon_{ui}$  for each strip  $i$ .

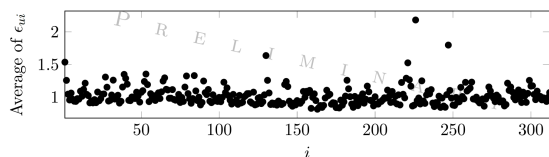


Fig. 6. Transverse geometric factors ( $g^{\text{tr}}$ ). The lines between data points illustrate the trend but do not refer to data interpolation. This result is Monte Carlo-based only due to the lack of a dedicated measurement.

Figure 6 shows the transverse geometric factors  $g^{\text{tr}}$ . Low values for large radial distances show that efficiency is higher near the edge of the field of view, as expected from the geometry of the detector strips, due to the LOR obliqueness.

#### 4. Conclusions

Normalization components highlight the relative importance of several physical and geometrical effects. They can be used to obtain insights of the efficiency of different aspects of the scanner, such as detector efficiency or the scanner response with respect to LOR obliqueness. Due to the design of the J-PET scanner, in which the detector strips are axially continuous, the definition of some normalization factors must be adapted. Future work

will consist of interpolating the normalization factors, which have an axial dependency, to compute the normalization factors for any point along the whole strip, and to assess the improvements in image quality taking into account all normalization factors during image reconstruction. The final goal is to apply the same procedure to the future Total-Body J-PET scanner [10, 11].

#### Acknowledgments

The authors acknowledge the support provided by the Foundation for Polish Science through the TEAM POIR.04.04.00-00-4204/17 program; the National Science Centre of Poland through grants MAESTRO no. 2021/42/A/ST2/00423 and OPUS no. 2019/35/B/ST2/03562; the Ministry of Education and Science through grant no. SPUB/SP/490528/2021; the SciMat and qLife Priority Research Areas budget under the program *Excellence Initiative — Research University* at the Jagiellonian University, and Jagiellonian University project no. CRP/0641.221.2020.

#### References

- [1] L. Raczyński, P. Moskal, P. Kowalski et al., *Nucl. Instrum. Methods Phys. Res. A* **764**, 186 (2014).
- [2] P. Moskal, K. Dulski, N. Chug et al., *Sci. Adv.* **7**, eabh4394 (2021).
- [3] P. Moskal, A. Gajos, M. Mohammed et al., *Nat. Commun.* **12**, 1 (2021).
- [4] S. Niedźwiecki, P. Białas, C. Curceanu, *Acta Phys. Pol. B* **48**, 1567 (2017).
- [5] P. Moskal, P. Kowalski, R.Y. Shopa et al., *Phys. Med. Biol.* **66**, 175015 (2021).
- [6] *Positron Emission Tomography: Basic Sciences*, Ed. D.L. Bailey, Springer, New York 2005.
- [7] R.D. Badawi, P.K. Marsden, *Phys. Med. Biol.* **44**, 571 (1999).
- [8] A. Pépin, S. Stute, S. Jan, C. Comtat, in: *2011 IEEE Nuclear Science Symposium Conference Record, Valencia*, IEEE, 2011.
- [9] D. Sarrut, M Bała, M. Bardiès et al., *Phys. Med. Biol.* **66**, 10TR03 (2021).
- [10] P. Moskal, E.Ł. Stepień, *PET Clinics* **15**, 439 (2020).
- [11] A. Alavi, T.J. Werner, E.Ł. Stepień, P. Moskal, *Bio-Algorithms Med-Syst.* **17**, 203 (2021).